



Microstructural evolution of electrodes in sintering of multi-layer ceramic capacitors (MLCC) observed by synchrotron X-ray nano-CT



Gaku Okuma^{a,*}, Naoya Saito^b, Kotaro Mizuno^c, Yoshiki Iwazaki^c, Hiroshi Kishi^c, Akihisa Takeuchi^d, Masayuki Uesugi^d, Kentaro Uesugi^d, Fumihiro Wakai^b

^a Research Center for Structural Materials, National Institute for Materials Science (NIMS), Ibaraki, 305-0047, Japan

^b Laboratory for Materials and Structures Laboratory, Institute of Innovative Research, Tokyo Institute of Technology, Yokohama, 226-8503, Japan

^c Research and Development Laboratory, Taiyo Yuden Co., Ltd., Gunma 370-3347, Japan

^d Japan Synchrotron Radiation Research Institute, JASRI/SPring-8, Kouto 1-1-1, Sayo, Hyogo 679-5198, Japan

ARTICLE INFO

Article history:

Received 2 November 2020

Revised 20 December 2020

Accepted 23 December 2020

Available online 3 January 2021

Keywords:

Sintering

Synchrotron X-ray tomography

3D microstructure

MLCC

ABSTRACT

Synchrotron X-ray nano computed tomography was used to investigate the microstructural evolution during co-sintering of multi-layer ceramic capacitors (MLCC) consisting of Ni electrodes and BaTiO₃ dielectric layers stacked alternately. As the electrode thickness reduced to submicron at the scale of a few particle diameters, the process produced the defect of inner electrode leading to capacitance loss. The discontinuous electrode region contained round holes and irregularly-shaped channels. The formation of discontinuity was associated with the increase of characteristic length of heterogeneous electrode structure, i.e., the coarsening occurred. The evolution of electrode morphology by surface/interface diffusion caused the breakup of ligament between two holes driven by instability induced by surface tension and stress. The ligament pinch-off inevitably generated sharp points which might enhance the local electric field bringing about the dielectric breakdown. A model was presented to explain the formation of defect from the heterogeneous particles packing in the electrode layer.

© 2021 Acta Materialia Inc. Published by Elsevier Ltd.

This is an open access article under the CC BY-NC-ND license

(<http://creativecommons.org/licenses/by-nc-nd/4.0/>)

1. Introduction

Multilayer ceramic capacitors (MLCC) are widely used in electronic devices such as smartphones and automotive applications. As the modern electronic industry demands for miniaturization of MLCC consisting of metal electrodes and ceramic dielectric layers stacked alternately, the thickness of both layers has been reduced significantly in recent years. Such multilayer components are produced by tape casting of dielectric material, screen printing of the metal electrode on the ceramic layer, stacking layers, pressing, cutting/dicing into green chips, binder burnout, and co-firing in a reducing atmosphere. The microstructural evolution of the electrode layer and the dielectric layer during co-sintering affects capacitance, reliability and lifetime of final products [1].

Since the thickness of layer has been reduced to micrometer range, the process introduces the defect of inner electrode called as discontinuity, which is seen in cross-section perpendicular to the layers [2]. The electrode with the thickness about 1.2 – 2 μm

is not an ideal plate, but its structure is similar to a Swiss cheese slice. The morphology of discontinuity in a thin electrode layer was round or irregularly-shaped holes as observed by Samantaray [3] using FIB-SEM tomography and by Yan [4] using synchrotron X-ray nano-tomography.

The electrode morphology evolves by surface motion due to diffusion along surface and electrode/dielectric interface, which is driven by a chemical potential gradient arising from the surface/interface tension and the difference in curvature. The surface motion occurs toward decreasing the total surface energy. Nichols and Mullins [5] analyzed the break up, or pinch-off of a cylindrical rod by Rayleigh instability under surface diffusion. Yu and Wei [2] suggested that the discontinuity took place mainly by surface tension induced Rayleigh instability. Srolovitz presented a model that flat surface is unstable when the body is elastically stressed [6]. Sridhar, Rickman, and Srolovitz [7,8] predicted that the presence of internal or applied stresses modifies the microstructural stability of multilayers under interface diffusion. The breakup of a rod is also promoted by the effect of stress. The shape of a body changes toward decreasing the elastic strain energy. Under the stresses due to misfit strain, the ideal flat parallel plates are

* Corresponding author.

E-mail address: OKUMA.Gaku@nims.go.jp (G. Okuma).

unstable with respect to the growth of perturbation. The instability depends on the thickness ratio and the elastic constant ratio of two layers. The MLCC composed of base metal (Ni) electrode and the dielectric BaTiO₃ is unstable, because the elastic modulus of Ni is higher than that of BaTiO₃, and the thickness of dielectric layer is larger than that of the electrode layer. Polotai [9,10] suggested that the multilayer structures were unstable under internal stresses arising from differential shrinkage during co-sintering. The shrinkage of Ni electrode takes place at temperatures from 500 to 1000 °C. Since the shrinkage rate of electrode is faster than the dielectric layer, the strain rate mismatch gives rise to tensile stress in the electrode layer. The densification of dielectric BaTiO₃ layer occurs at higher temperatures above 1100 °C. The electrodes are under compression in this stage. A low-melting interfacial liquid (Ni, Ba, Ti) alloy layer with the thickness of 10 nm is formed at 1000 – 1100 °C. This interfacial liquid layer promotes the diffusion along the interface [10]. The stress induced instability promotes the diffusion from thinner regions toward thicker regions leading to the increase of roughness of the electrode layer and the formation of discontinuity. Polotai [10] confirmed that the continuity of Ni electrode could be improved by using fast-heating rate, which suppressed kinetically the formation of the interfacial liquid layer. The fast-heating rate decreases the temperature dependence of capacitance, and decreases the BaTiO₃ grain size, leading to longer lifetime [11].

The microstructural control for obtaining smoother and more continuous electrodes is important for improving the performance of MLCCs. The capacitance of MLCC is directly proportional to the continuity and connectivity of the electrode area, then the discontinuity brings about capacitance loss. The lifetime of MLCCs is limited by insulation resistance degradation under DC electrical field. The degradation is accelerated with increasing temperature. Chazono and Kishi [12] proposed a model that the impedance has contributions from the intragranular core-shell structure, grain boundaries, and the electrode interfaces. Yang [13] reported that the Schottky barrier formed at the interface between the Ni electrode and BaTiO₃ grains gives the largest contribution to the total insulation resistance. Samantaray [3] analyzed that the dielectric breakdown strength is lowered by the enhancement of local electric field arising from electrode discontinuities and rough interfaces, because the local leakage current density along the electrode-dielectric interface is enhanced by the high local electric field. The thickness of a dielectric layer and the local electric field in it vary with the roughness of two electrodes adjacent to the dielectric layer [14]. Sharp intrusions of the electrode into the dielectric layer should be avoided to reduce the device breakdown [15].

The understanding of microstructure evolution during co-sintering is necessary to control the morphology of electrode layer. Yan and coworkers systematically investigated the microstructural evolution of MLCC with the electrode thickness of micrometer range by using in-situ synchrotron X-ray microtomography [4,16] and FIB-SEM nanotomography [17]. They presented a schematic model for the formation of discontinuity and the increase of electrode roughness [4]. Some particles in low density regions desinter [18], i.e., bonded particles are separated due to tensile force or constraint [19], and large pores appear. Finally, pores enlarge and lead to discontinuous areas in electrode layer. The evolution of defects in electrode was simulated by discrete element method (DEM) [20], which was able to analyze the internal stress during co-sintering and the de-sintering. But the predicted defect structure was different from the morphology of discontinuity observed by X-ray microtomography, probably because DEM simulation could not take account of the effect of Rayleigh instability and stress induced instability.

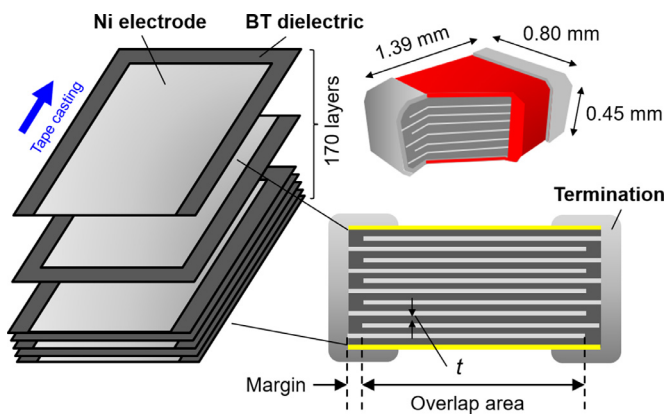


Fig. 1. Schematic illustration of internal structure of MLCC.

Recently Takeuchi and co-workers [21] at SPring-8 synchrotron facility developed a multiscale X-ray computed tomography consisting of an X-ray microtomography as a wide-field and low-resolution system and a phase-contrast high-energy X-ray nanotomography as a narrow-field and high-resolution system. This imaging tool is suitable to reveal the complicated three-dimensional morphology of defects evolved during sintering of ceramics [22]. Here we used the X-ray nanotomography to investigate the microstructural evolution of MLCC. The aim of this work is to obtain a further understanding of complex three-phase microstructures (electrode, dielectric, and pore), and to provide a new quantitative description of microstructural features for improving the performance of MLCC. In downsizing the MLCC, the properties are affected by physical dimensions. This effect is referred to size effect or scaling effect [23]. With decreasing the electrode thickness to submicron range, there are only a few Ni particles in the thickness direction. For the electrode with thickness below 1 μm, the initial electrode structure is intrinsically heterogeneous due to packing structure in particle scale. We show that the discontinuity evolves together with the coarsening of a characteristic length which represents the heterogeneity of electrode microstructure.

2. Experimental

The model MLCC chips with 1005 size (1.0 mm × 0.5 mm × 0.5 mm) were used as samples in this work (Fig. 1). The model MLCC was fabricated by TAIYO YUDEN CO., LTD., Gunma, Japan in a condition where the discontinuity was formed readily, in order to investigate the formation mechanism. The dielectric powder of BaTiO₃ (barium titanate, BT) with a mean particle size of ~200 nm was mixed with additives such as SiO₂ that form a liquid phase during sintering, solvents, dispersant, binder, and plasticizers. The slurry was tape casted to a thin continuous sheet using a doctor blade (tape casting direction is shown in Fig. 1). After the drying process of the wet sheet, a paste containing Ni particles (~200 nm) and 10 wt% nano sized BT particles (~50 nm) was applied to the tape via screen printing. The nano sized BT particles are added to retard the densification rate of metal layer, so that the sintering temperature for metal layer is adjusted to be closer to that for dielectric layer [24]. The printed tape was then stacked layer by layer, followed by cutting into the individual green MLCC chips with a size of 1.39 mm × 0.80 mm × 0.45 mm. There were 170 layers in the model MLCC chip. The binder burnout was conducted at a heating rate of 15 °C/h up to 270 °C. The green chips were non-isothermally sintered under a heating/cooling profile with the maximum rate over 10000 °C/h in a reducing atmosphere using a N₂ and H₂ gas mixture. Four different MLCC chips were prepared

at maximum temperatures ranging from 800 °C to 1250 °C. Samples were machined with a pen type mini router into elongated trapezoidal plates with thickness of 25 μm at the tip for ex-situ observation by nano-CT.

The synchrotron X-ray nano-CT at BL20XU of the Japanese synchrotron radiation facility, SPring-8, was used to study the 3D internal structure of MLCC. Experimental setup for nano-CT have been fully described in Ref. [21]. X-ray energy was set at 20 keV. Optical system of nano-CT mode is based on a phase contrast X-ray full-field microscope. A hollow-cone illumination system using a condenser zone plate (CZP), sample stages, a Fresnel zone plate (FZP) objective, and a Zernike phase plate (phase ring) are placed at the experimental hutch 1 of the BL20XU. A visible-light conversion type X-ray image detector (C12849-SY69701, Hamamatsu Photonics) is installed at the 2nd hutch located ~160 m downstream from the 1st hutch. The sample was rotated by steps of 0.1° up to 180°. Voxel sizes for nano-CT is 50 nm, and the measuring time for one sample is 8 min.

The 3D mappings were reconstructed from the acquired data by using the filtered back-projection method. The 3D visualization and geometrical measurements were performed using Amira (VSG, Burlington, Massachusetts, USA), and a Gaussian filtering was applied to reduce the noise in 2D images. Local thresholding method was used to segment the gray value image into defect and material, so as to determine the defect size. The surface was discretized using triangular meshing, from which the volume and surface area of electrodes and pores were calculated.

3. Results

3.1. Multilayer structure observed in the cross-section

Fig. 2 shows the evolution of multilayer structure observed in the cross-section perpendicular to the layers by scanning electron microscopy (SEM). Here, BT dielectric, Ni electrode, pore spaces are shown in gray, white, and black, respectively. The sintering of Ni particles occurred already at 800 °C (**Fig. 2 (a)**), while BT particles were not sintered yet. The Ni electrode consisted of short segments which were divided by many small gaps between them. The electrode was not continuous, so that the discontinuity appeared in this early stage. The surface of Ni electrode was covered with nano sized BT particles, which was kept out of the sintered Ni metal (**Fig. 2 (a), (i)**). The contact areas among BT particles were formed at 1000 °C (**Fig. 2 (b)**). The grain growth took place in Ni electrode. The pores near the electrode layer were located at discontinuities. The electrode was partially detached from the BT layers forming the interfacial pore between the electrode layer and the BT layers (**Fig. 2 (b), (ii)**). The BT layers densified further at 1150 °C (**Fig. 2 (c)**). Several small circular Ni electrode segments were observed in the porous region (**Fig. 2 (c), (iii)**). The BT layers were almost fully densified at 1250 °C (**Fig. 2 (d)**). The electrode layer was brought back in contact with the BT layers, so that the interfacial pores between the electrode and the BT layer disappeared. Pores remained at discontinuities of Ni electrode. Some parts of discontinuities were filled by BT grains. A few very small spherical particles inside Ni electrode were nano sized BT particles entrapped in it (**Fig. 2 (d), (iv)**).

The porosity in BT layer was measured from the micrographs, and plotted in **Fig. 3 (a)**. The densification of BT layer occurred at temperatures higher than 1000 °C, and gave the volumetric strain of -35% at 1250 °C, which corresponded to isotropic linear shrinkage of 13%. On the other hand, the thickness of BT layer decreased from 1.57 μm at 800 °C to 1.25 μm at 1250 °C as shown in **Fig. 3 (b)**. The shrinkage about 20% in the thickness direction was much larger than that expected from the isotropic shrinkage. The

shrinkage occurred in the thickness direction mainly, because the lateral shrinkage of BT layer was constrained by the electrode layer.

The electrode discontinuity was defined by the total length of gaps in electrode layers

$$\text{Discontinuity (\%)} = 100 \times \sum_{i=1}^m L_{di}/L_0 \quad (1)$$

where L_0 is the observed length, L_{di} denotes the length of each gap between electrode segments, and m is the total number of gaps (**Fig. 2 (c)**). The discontinuity was already formed at 800 °C, and increased to about 40% at 1250 °C as shown in **Fig. 3 (c)** (solid line). The growth of gap length correlates with the decrease of length of electrode segments. As the segment length was reduced, the electrode thickness increased from 480 nm at 800 °C to 780 nm at 1250 °C (**Fig. 3 (b)**). The gap consists of pore (void or cavity), or it is filled with BT grains. The contribution of pore to the total discontinuity was also plotted in **Fig. 3 (c)** (dotted line). The discontinuity in the electrode layer was mainly made of pore at 800 °C, but a significant part of the discontinuity was filled with BT grains at 1250 °C. It is supposed that nano sized BT particles dispersed in the electrode layer filled the discontinuity partly.

3.2. Multilayer structure observed by X-ray nanotomography

3.2.1. Coarsening process of electrode microstructures

The regions near the boundary between the overlap electrode area and the margin (**Fig. 1**) were observed by X-ray nanotomography. **Fig. 4** shows a top view of the Ni electrode layer observed by X-ray nanotomography. We could not observe the electrode structure of a sample sintered at 800 °C, probably because the dispersion of nano sized BT particles, the size of which was less than the resolution of nano-CT, made it difficult to discern Ni electrode from BT layer clearly. Thin electrode layer with the initial thickness of 500 nm is porous, where Ni regions (magenta) are connected with ligaments or bridges to form complicated network structures. Some electrode islands are isolated from other electrode regions, and colored in cyan. Pores and BT grains are transparent, so that black background indicates the discontinuity. The discontinuous regions are small round holes or irregularly-shaped channels. The ratio of the black background area to the total area was defined as discontinuity, and plotted in **Fig. 3 (c)** (dashed line). Therefore, the coverage of electrode, the ratio of electrode area to the total area, is $(100 - \text{discontinuity})\%$. The discontinuity obtained by X-ray CT agreed with the discontinuity calculated from the SEM observation fairly well.

It is clearly seen that the characteristic length of electrode and discontinuity increases with sintering temperature, that is, the morphological evolution of electrode microstructure is described as coarsening. We used three methods to define the characteristic length; (1) the average intercept length, (2) the average discontinuity length, and (3) the inverse of specific area. The average intercept length l was calculated from the electrode boundary in **Fig. 4**.

The average discontinuity length $\bar{L}_d = \sum_{i=1}^m L_{di}/m$ was measured from SEM micrographs (**Fig. 2**). The specific surface area S_V was calculated as the ratio of electrode surface area S to electrode volume V . We used the inverse of S_V as characteristic length $1/S_V$ [25]. The relation between the characteristic length and sintering temperature is shown in **Fig. 5**. The coarsening is described quantitatively by the increase of the average intercept length and the average discontinuity length with sintering temperature. For nanoporous metals, the total surface energy decreases in the coarsening due to surface diffusion driven by surface tension. The inverse of specific surface area of nanoporous metals, then, increased with self-similar coarsening [26]. However, $1/S_V$ of the electrode in **Fig. 5** did not

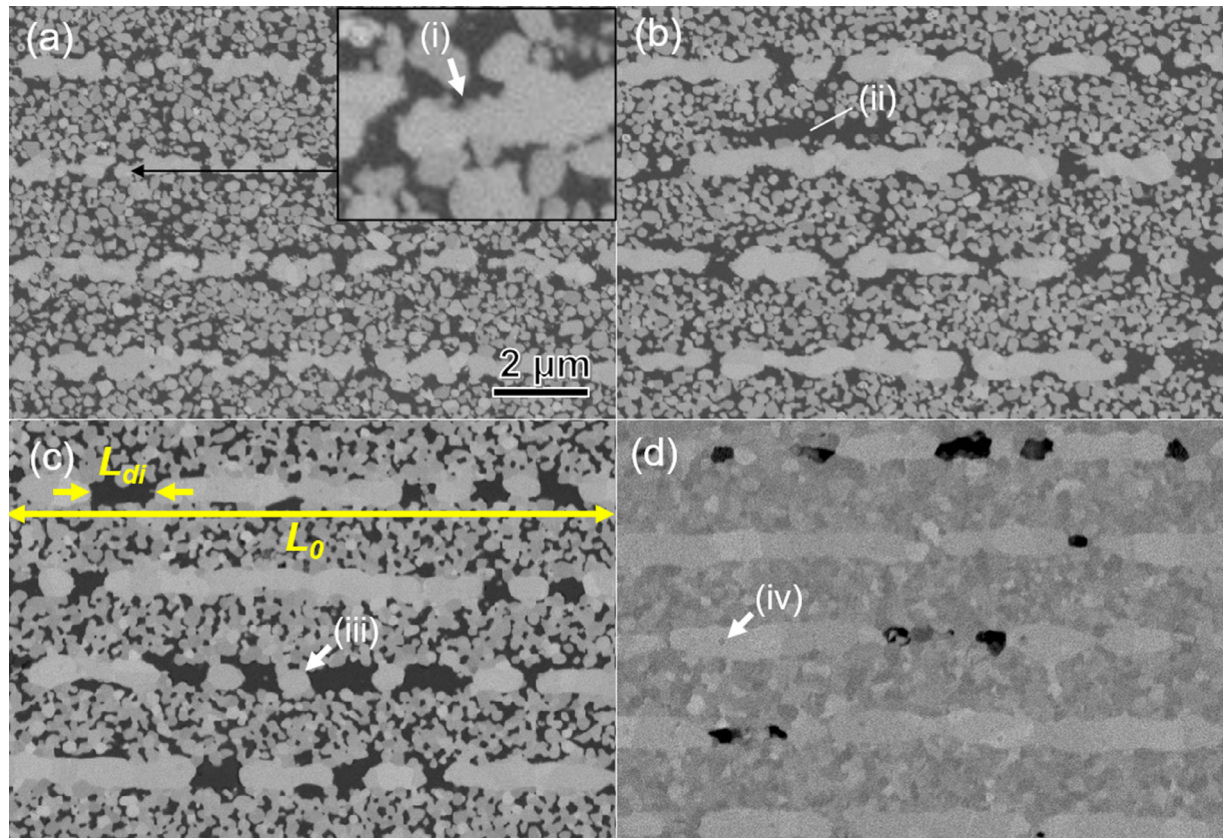


Fig. 2. SEM micrographs of MLCC observed in the cross-section perpendicular to layers. Sintering temperatures; (a) 800 °C, (b) 1000 °C, (c) 1150 °C, (d) 1250 °C. Some characteristic features are indicated; (i) nano sized BT particles, (ii) a pore along interface between the electrode layer and the BT layer, (iii) a circular cross section of a ligament, (iv) nano sized BT particles entrapped inside the electrode.

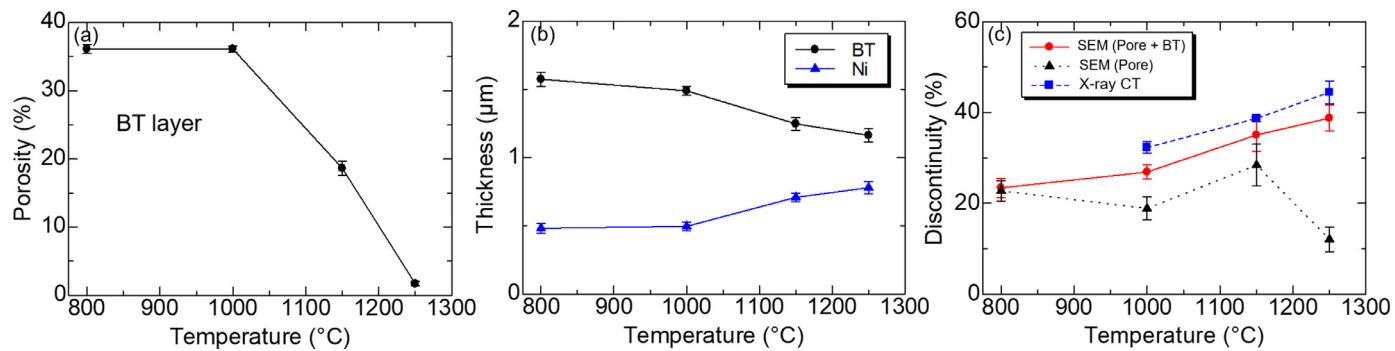


Fig. 3. Relation between microstructural features and the sintering temperature. (a) porosity in dielectric BT layer, (b) thicknesses of BT layer and Ni electrode layer, (c) discontinuity.

increase significantly at temperatures higher than 1150 °C. This result suggests that the coarsening of electrode is related to other driving force besides surface tension, for example, the stress driven instability at the temperature range between 1100 °C and 1250 °C where the electrode is under compression.

The details of microstructural evolution are shown in Fig. 6 (a), (b), (c), where the regions bounded by dashed rectangles in Fig. 4 are magnified. The coarsening of a hole takes place by the coalescence of two round holes. It occurs by pinch-off of the ligament between hole (h1) and hole (h2) in Fig. 6 (b). The hole (h3) will be connected to the irregularly-shaped channel (ch1) by the pinch-off of the ligament between them. The branched channel (ch2) in Fig. 6 (c) is formed by the coalescence of several irregularly-shaped channels. The process of ligament pinch-off produces many sharp points, for example, points (p1 and p2) in

Fig. 6 (c). A round hole is made by merging small embryonic holes in the dashed rectangle in Fig. 6 (b). The hole (h4) shows the shape after the coalescence of two small holes.

3.2.2. Pore structures in electrode layer

The distribution of pores (shown in yellow) in the electrode layer is illustrated in Fig. 6 (a1), (b1), and (c1). The pores are located at discontinuities such as holes and channels. Even though two discontinuities are separated by a ligament between them, the pore (po1 in Fig. 6 (a1)) located at them is connected. The pore covering the electrode is seen as interfacial pore between electrode and dielectrics by SEM observation on the cross-section (Fig. 2 (b), (ii)). The pore structure is described as a network of pore channels at the sintering temperature of 1000 °C (Fig. 6 (a1)). The pinch-off of pore channels and pore coarsening are accompanied with

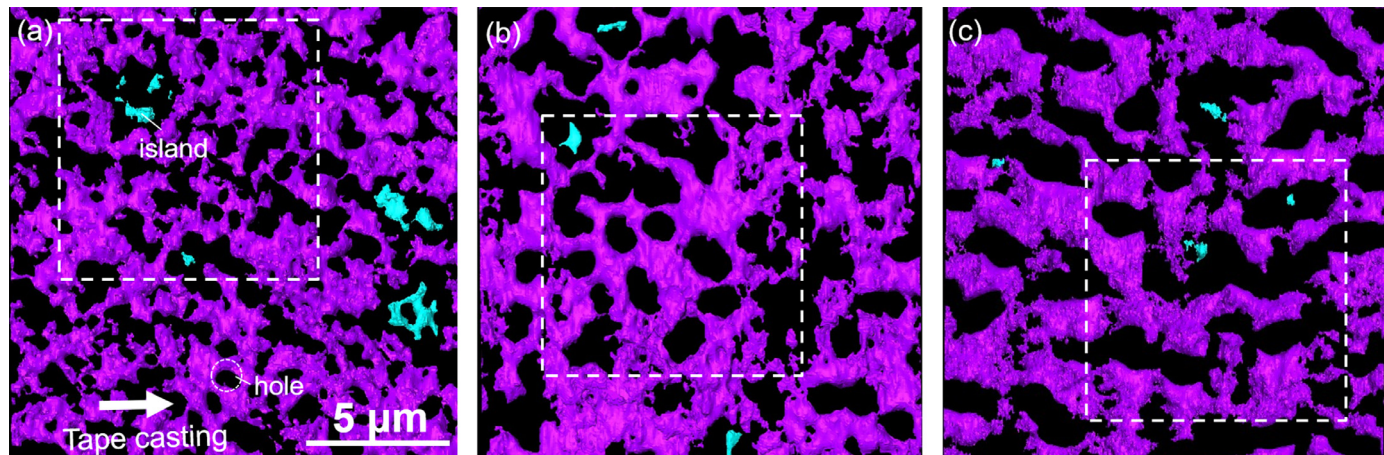


Fig. 4. Distribution of Ni metal in an electrode layer. Sintering temperatures; (a) 1000 °C, (b) 1150 °C, (c) 1250 °C. The continuous electrode region is shown in magenta, while isolated regions (islands) are shown in cyan. The discontinuities are seen as black background.

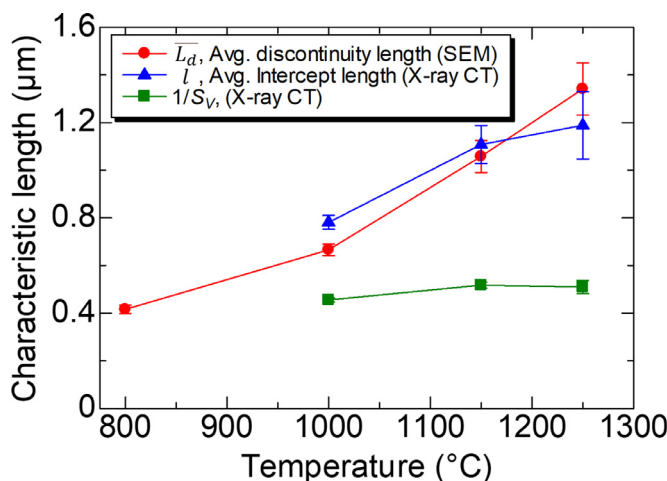


Fig. 5. Relation between characteristic lengths and sintering temperature. The microstructural evolution of electrode layer is described as the coarsening of characteristic lengths.

the coarsening of electrode structure at 1150 °C (Fig. 6 (b1)). The black background in Fig. 6 (b1) shows that the holes (h_1, h_2, h_3 in (b)) are not filled by pores completely, but there is an interfacial layer of BT phase between Ni electrode and the pore. The interfacial layer of BT phase is formed by sintering of nano BT particles which covered the surface of Ni electrode (Fig. 2 (a), (i)). Since the interfacial layer of BT phase sinters with BT particles on both sides of an electrode, two BT layer are connected by the interfacial layer. At 1250 °C (Fig. 6 (c1)), large closed pores remain in the electrode layer, while fine pores in BT layer disappear almost completely. With increasing the discontinuity area, a significant part of the discontinuity is filled by BT grains as indicated by the growth of black background area.

While the electrode volume is conserved during coarsening, the pore volume in the electrode layer decreased during the sintering. The electrode volume per unit area was constant, 0.22 μm, that is equivalent to the thickness of an ideal flat electrode layer. The pore volume per unit area was 0.22 μm and 0.14 μm at 1000 °C and 1250 °C, respectively. The volume fraction of pore in the electrode layer was almost the same with that of metal at 1000 °C. The coarse closed pores remained at 1250 °C, because its shrinkage was constrained by the metal electrode.

3.2.3. Interface roughness of electrode

The electrode layer was cut along dashed lines in Fig. 6 (a1), (b1), and (c1). The side view of the electrode is displayed in Fig. 6 (a2), (b2), and (c2). The discontinuity and the interface roughness of electrode affects the enhancement of local electric field and the leakage current [14]. The characteristic feature of surface roughness is the presence of protrusions of the electrode extending into the dielectric layer (Fig. 6 (c2)). These spikes look like sharp points formed after the pinch-off of ligaments (Fig. 6 (c), p1 and p2), but locate in the out of plane orientation. Heath [15] showed that the enhancement of electric field was the maximum at such local features by FEM simulation. He suggested this structure would likely lead to device breakdown.

Although the pore structure near the electrode is connected to fine network of open pores in BT layer in Fig. 2, the fine pores inside BT layer could not be imaged by synchrotron X-ray nanotCT. The pore connectivity is only suggested by several pillars of pore protruding toward the BT layer from the electrode layer in Fig. 6 (a3) and (b3). The cross-sectional view (a4), (b4), (c4) corresponds to SEM micrographs in Fig. 2. The pore at the interface between electrode and BT phase ((a4) left hand) is a cross-section of a connected pore (po2 and po3 in (a1)). Small circular Ni electrode segments observed in Fig. 2 (c), (iii) is a cross-section of a rod-like ligament (Fig. 6 (b4), Lig). Interfacial layers of BT phase were observed between the ligament and pores on both sides.

3.2.4. Topological evolution of Ni metal and pores in electrode layer

The topology of a surface of connected electrode is characterized by genus g , roughly speaking, it is the number of holes in the surface. A single sphere has $g = 0$, and a torus (doughnut shape) has $g = 1$. When a ligament between two adjacent holes is pinched-off, two holes coalesce into a single larger hole. The microstructure evolution in coarsening of electrode structure is expressed as the decrease of genus one by one through this topological transition. Fig. 7 (a) shows the genus of electrode per unit area decreases with increasing the sintering temperature. The comparison of Fig. 7 (a) with Fig. 5 indicates the correlation between the topological transition and the coarsening of characteristic length. Such topological relationship is also reported by Erlebacher for the coarsening of nanoporous metals [27]. Mendoza analyzed the interfacial topology during coarsening of uniaxially solidified metals also [28].

On the other hand, the topological evolution of pore channels is different from that of Ni metal electrode. The network of pores is broken into large closed pores at 1250 °C. The topology of con-

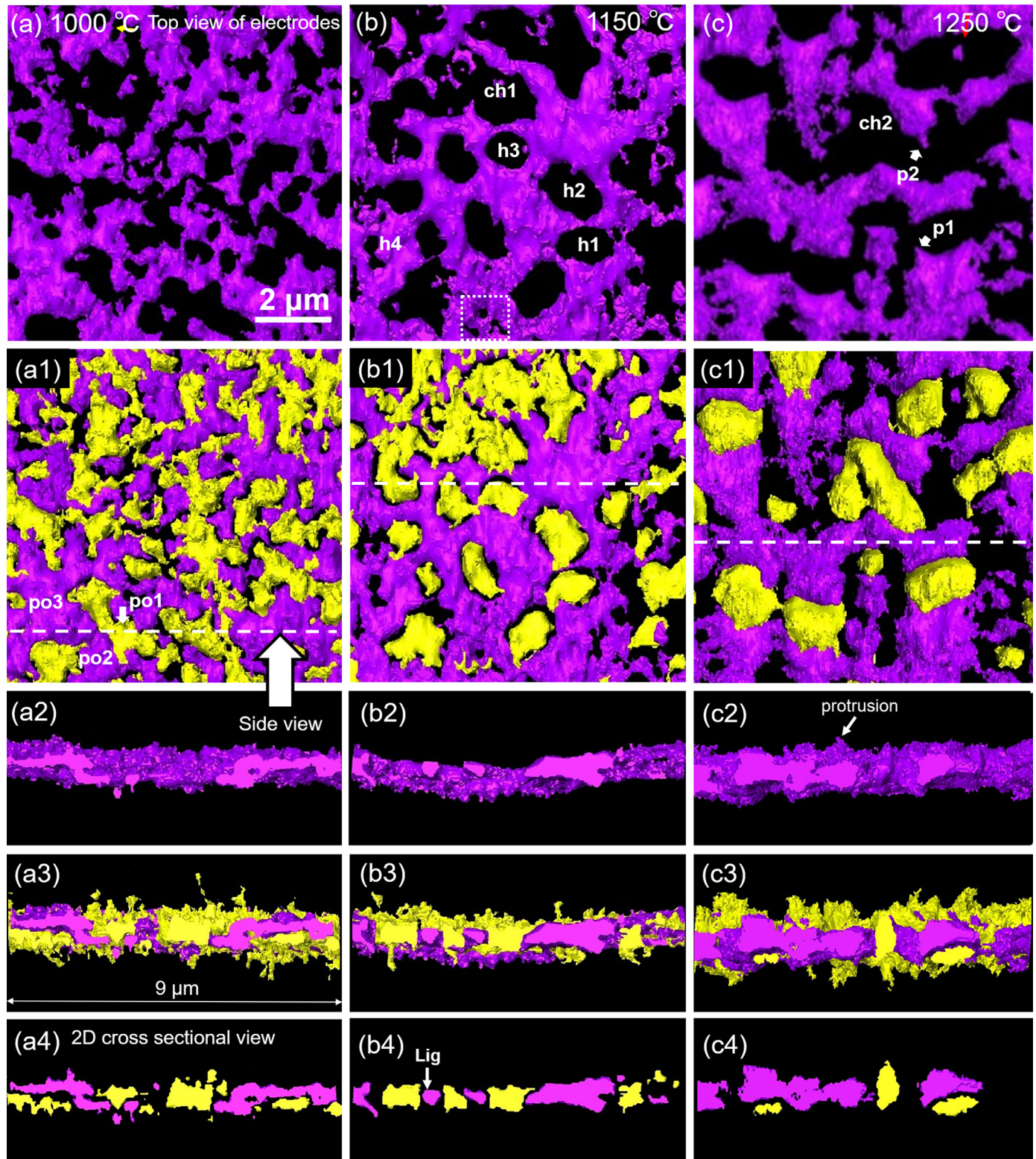


Fig. 6. Microstructural evolution of electrode layer. Sintering temperatures; (a) 1000 °C, (b) 1150 °C, (c) 1250 °C. (a), (b), (c); top view, Ni electrode. (a1), (b1), (c1); top view, Ni electrode and pores. (a2), (b2), (c2); side view, Ni electrode. (a3), (b3), (c3); side view, Ni electrode and pores. (a4), (b4), (c4); 2D cross-sectional view.

nected pore channels and closed pores is described by using the half of total Euler characteristic as a sum of Euler characteristics of all pores [29]

$$X/2 = \sum_{n=1}^N (1 - g) \approx N - G \quad (2)$$

where N is the number of pores, and G is the sum of genus $\sum g$. The advantage of Euler characteristic is that it takes account of the number of closed pores. Okuma [30] proposed that the stages of sintering could be distinguished from the interface topology by using the Euler characteristic. The Euler characteristic is calculated

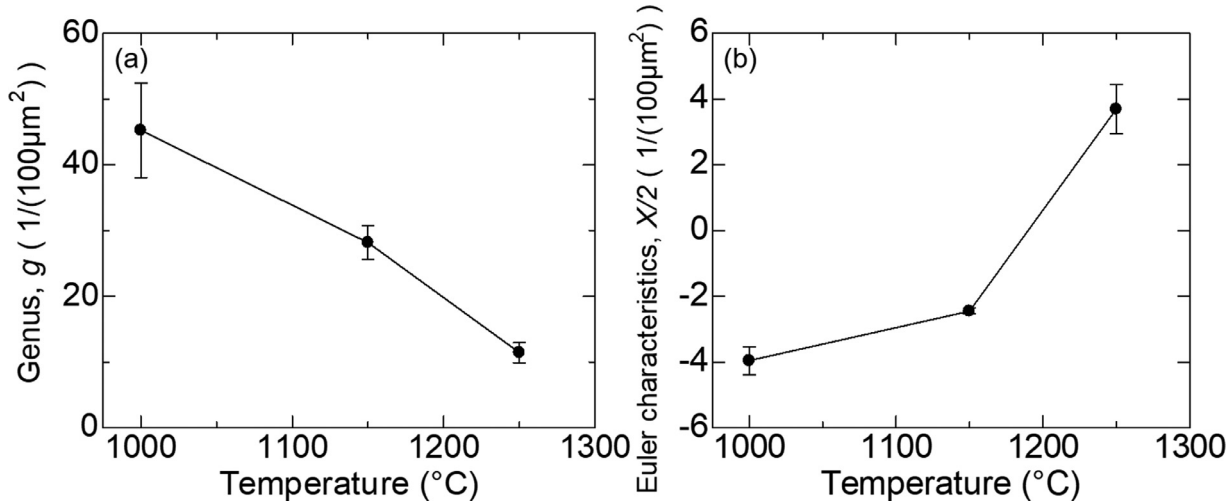


Fig. 7. Topological evolution of electrode layer. (a) Genus (G) of Ni electrode per electrode area of $100 \mu\text{m}^2$, (b) Euler characteristic ($X/2$) of pores in the electrode layer per electrode area of $100 \mu\text{m}^2$.

from the tomography data by using the Gauss-Bonnet theorem

$$X/2 = \frac{1}{4\pi} \int_A K dA \quad (3)$$

where $K = \kappa_1 \kappa_2$ is the Gaussian curvature. $X/2$ per unit area of pore structure in the electrode is presented in Fig. 7 (b). The porous electrode structure is bicontinuous up to 1000°C , where the network of pore channels is described as a collection of holes. The Euler characteristic is negative at 1000°C , since the number of holes in pore channel is larger than the number of closed pores. The Euler characteristic increases with the pinch-off of pore channels and the formation of closed pores. It is positive when only closed pores remain at 1250°C .

3.2.5. Capacitance loss by discontinuity and isolated islands

The capacitance of a MLCC is given by

$$C = \varepsilon_0 \varepsilon'_r (n - 1) S / t \quad (4)$$

where S is the overlap electrode area of internal electrode, t is the thickness of the single dielectric layer, n is the number of layers, ε_0 is the vacuum permittivity, and ε'_r is the relative dielectric permittivity. The dielectric constant of BaTiO_3 depends on temperature, rare-earth doping [1], electric field, grain size [23], and residual stress [31]. The electrode discontinuities modifies the electric field distribution in dielectric layer [14]. Furthermore, there are isolated islands in the electrode (colored in cyan in Fig. 4). The authors suppose that both discontinuities and the isolated islands reduce the effective overlap electrode area, so that the capacitance will be lower than that of ideal parallel electrode plates.

4. Discussions

4.1. Possible factors affecting the formation of discontinuity

The evolution of discontinuity in Ni electrode was described as the coarsening of characteristic length from the comparison of Figs. 3 (c) and 5. While coarsening of porous structure took place by surface/interface diffusion driven by surface tension usually, the specific surface/interface area did not decrease significantly by the formation of discontinuity. This result supports that the thermodynamic instability of layered structure under stress is the origin of morphological evolution of electrode. This model provides several approaches for controlling the discontinuity. The theoretical

analysis predicts that the instability is determined by the selection of thickness ratio and the elastic constant ratio of two layers [7,8]. The co-sintering at high heating rate is a kinetic approach to improve the continuity of electrode by suppressing the formation of interfacial liquid layer at temperatures between 1000°C and 1100°C [10]. Here we discuss other factors, which may affect the formation of discontinuity.

As the thickness of electrode layer reduces to submicrometer scale, there are only a few particles in the thickness direction as shown in Fig. 2 (a). The electrode structure was heterogeneous, and many small gaps were already formed at early stage. The evolution of discontinuity was related to the coarsening of the average gap length, i.e., the average discontinuity length \bar{l}_d in Fig. 5. Therefore, we suppose that the distribution of small gaps and heterogeneity in the initial particle packing structure of electrode layer may affect the coarsening process. Konishi [32] reported that the formation of discontinuity could be suppressed with decreasing the ratio of Ni particle size (d) to electrode thickness (t_{Ni}). It is natural that the microstructure of an electrode layer becomes more homogeneous with decreasing d/t_{Ni} , in other words, with increasing the number of particles in the thickness. The local fluctuation of packing density is characterized by its standard deviation normalized by macroscopic density [33]. Okuma [34] studied the local fluctuation of relative density as a function of size of volume element in the sintered glass sphere compact by synchrotron X-ray computed tomography. The standard deviation of relative density increased significantly with decreasing the size of volume element. For the normalized standard deviation less than 2–5 %, the edge length of cubic volume elements must be 11–17 times larger than the particle size. This result agreed with the values reported for granular materials [35]. More recently, Fernandes [36] reported the heterogeneity of the microstructure increased for volume elements containing less than 80 particles. If the heterogeneity of thin electrode is defined based on a volume element with the size of layer thickness, it is predicted that the initial microstructural heterogeneity, and then, the microstructural instability will be pronounced with decreasing the ratio of electrode thickness to particle size less than 10, especially, less than 5. This analysis explains the effect of d/t_{Ni} on discontinuity formation.

In Fig. 8, we present an image of particle packing structure, for the case where the layer thickness decreases to only a few times larger than the particles size. As the initial Ni particle size was too small to observe by nanotomography, we illustrate a model structure for packing of spherical glass particles observed by X-ray mi-

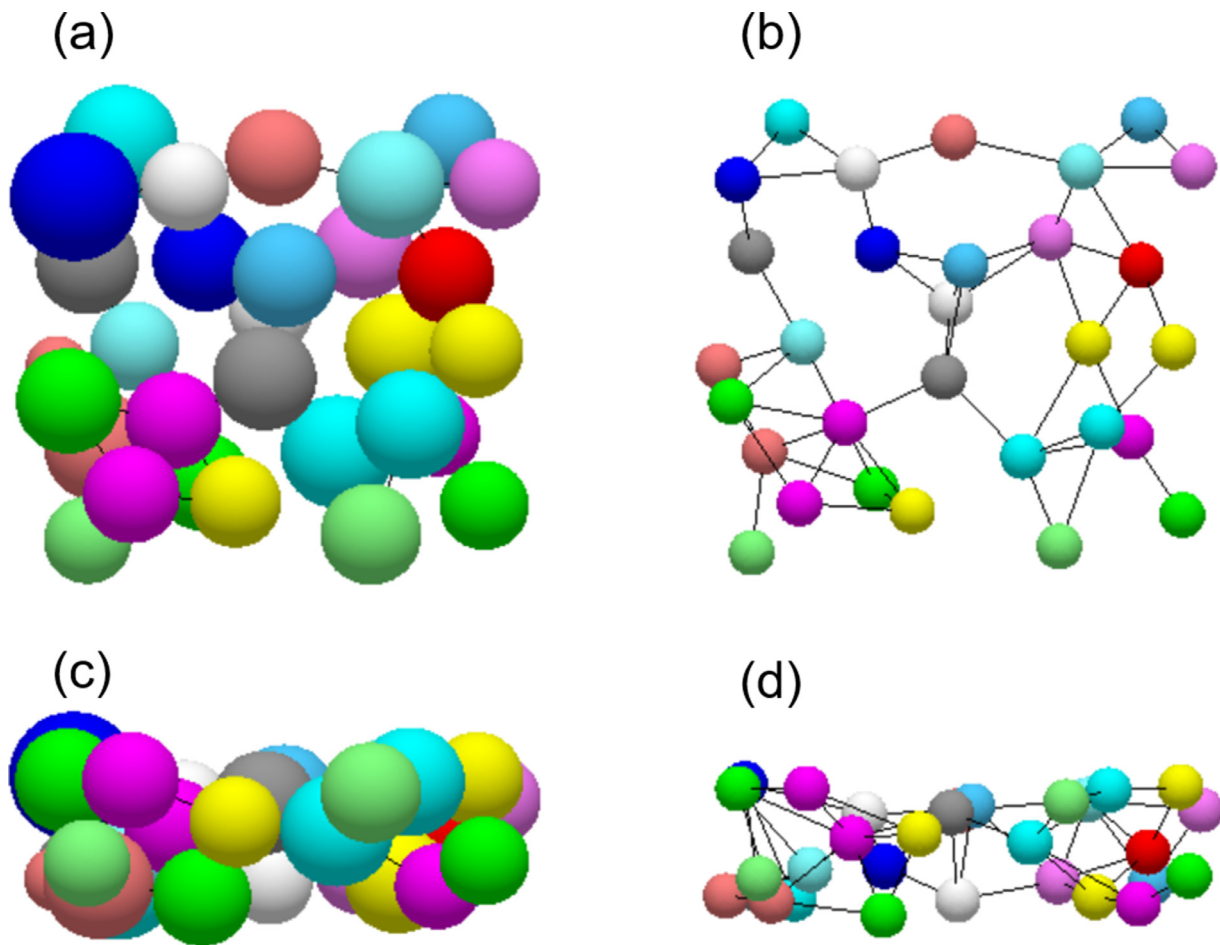


Fig. 8. A model of particles packing in thin electrode layer. Top view, (a) sphere model, (b) bond network model. Side view, (c) sphere model, (d) bond network model.

crotomography [30]. Fig. 8 (a) and (c) show the top view and the side view, respectively. It is seen that small gaps at particle scale present in the thin layer. The detailed structure of small gaps can be recognized by using the bond-network model [37] in Fig. 8 (b) and (d). A point represents each particle. A contact between two particles is represented by an edge between the representative points. A face is defined by a polygon composed of these vertices and edges. The irregular bond network can be characterized by a combination of faces. There is a hole at the center of each face, then, the sintered layer structure will be made of continuous networks containing numerous holes. The hole size increases with the number of edges of a polygonal face. We suppose that such small embryonic holes in thin electrode layer grow under constraint during co-sintering, leading to large holes in the electrode as follows: The shrinkage of an electrode layer is constrained by two dielectric layers on both sides in the early stage of sintering at temperatures less than 1000°C. This constraint effect will affect all Ni particles in the thin electrode layer. When Ni particles cannot rearrange easily, the local tensile stress will be generated in the electrode layer under constraint leading to the opening of small embryonic holes. Many small gaps are formed in the early stage of co-sintering in this way.

4.2. Partial-wetting in sintering of Ni particle and BaTiO₃ particle

The sintering between metal and ceramics, in the present case, Ni particle and BT particle, takes place when

$$\gamma_{NiBT} < \gamma_{Ni} + \gamma_{BT} \quad (5)$$

where γ_{Ni} is the surface energy per unit area for Ni phase, γ_{BT} is the surface energy per unit area for BT phase, and γ_{NiBT} is the energy per unit area for Ni/BT interface. The inset of Fig. 9 is a schematic illustration of structure at discontinuity of electrode layer. From the force balance in equilibrium, γ_{Ni} , γ_{BT} , and γ_{NiBT} are determined from the dihedral angle ψ , the contact angle ψ_{Ni} , and the contact angle ψ_{BT} by using Young's equations.

$$\frac{\gamma_{NiBT}}{\sin\psi} = \frac{\gamma_{BT}}{\sin\psi_{BT}} = \frac{\gamma_{Ni}}{\sin\psi_{Ni}} \quad (6)$$

The angles ψ , ψ_{Ni} , and ψ_{BT} were measured from SEM micrographs in Fig. 2. The surface energies are scaled to form two dimensionless ratios γ_{BT}/γ_{Ni} and $\gamma_{NiBT}/\gamma_{Ni}$. The measured dimensionless ratios are plotted in Fig. 9, which shows a wetting phase diagram of sintering in γ_{BT}/γ_{Ni} versus $\gamma_{NiBT}/\gamma_{Ni}$ space [38]. The scatter in the data arises as both surface energy and interface energy depend on crystallographic orientation. When the contact angle ψ_{BT} becomes zero, Ni phase is covered by BT phase, or BT phase wets completely at

$$\gamma_{Ni} \geq \gamma_{BT} + \gamma_{NiBT} \quad (7)$$

There are three distinct regions in the wetting phase diagram in Fig. 9; (i) complete wetting, (ii) partial wetting, and (iii) complete drying. The boundary between the complete wetting and the partial wetting is expressed by Eq. (5), and that between the partial wetting and the complete drying is expressed by Eq. (7). The contact angle ψ_{BT} is zero at complete-wetting, and is 180° at complete-drying in Fig. 9 (a). The average contact angle ψ_{BT} was from 118.3°, 118.8°, and 104.6° at 1000 °C, 1150 °C, and 1250 °C,

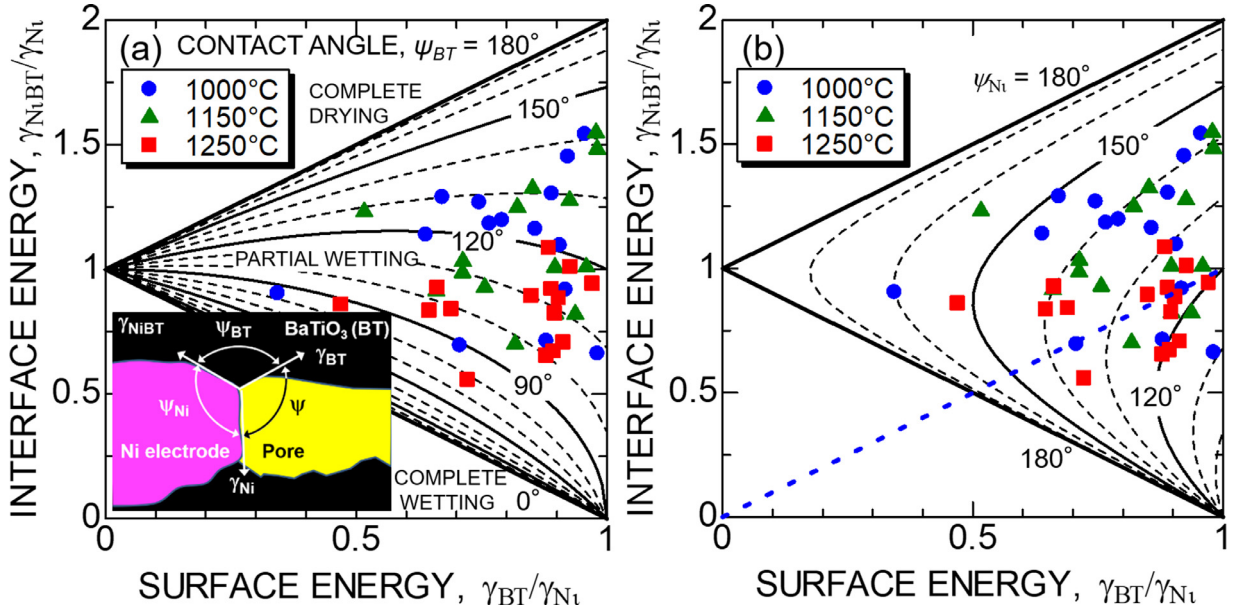


Fig. 9. Wetting phase diagram of sintering. (a) contact angle for BaTiO₃, (b) contact angle for Ni. The dotted line shows the expel/entrap boundary for nano BT particles from/in the Ni electrode (Eq. (8)).

respectively. All data were in the partial-wetting region, not in the region of complete wetting. In Fig. 9 (b), the average contact angle ψ_{Ni} for Ni was from 136.8°, 134.5°, and 130.6° at 1000 °C, 1150 °C, and 1250 °C, respectively. Wang studied the wettability between electrode metals and BaTiO₃ [39]. The contact angle was 128°, 116°, and 93° for Ag, Au, and Cu, respectively. The contact angle decreased with increasing temperature.

A free nano BT particle is energetically more stable than the entrapped one inside Ni electrode when

$$\gamma_{NiBT} > \gamma_{BT} \quad (8)$$

The dotted line in Fig. 9 (b) show the stability boundary of Eq. (8). Since the most of the data, especially at 1000 °C, lie above the dotted line, the most of nano BT particles are not entrapped inside Ni electrode. They remain on the Ni electrode surface. Thin interfacial layers of BT phase were observed between the Ni ligament and pores in the electrode layer in Fig. 6 (b1) and (b4) (interfaces between "Lig" and pore). This layer can be seen also in high resolution SEM micrograph (Fig. 3 (b) in Ref. [17]). Although such thin BT layer looks like the complete wetting of Ni electrode by BT phase, it is not formed by the thermodynamic equilibrium. The observation of contact angle ψ_{BT} supports the model that the thin layer was formed by sintering of nano BT particles on the metal surface.

4.3. Anisotropic structure of electrode layer

The anisotropic thermodynamic driving force in sintering of a porous body is related to the surface energy tensor, which is defined by

$$S_{ij} = \frac{1}{2} \int_A \gamma_s (\delta_{ij} - n_i n_j) dA \quad (9)$$

where γ_s is the surface energy or the interface energy, n_i is the unit normal to the surface, A is the surface area of the body [40]. The quantity S_{ij}/γ_s is simply determined from geometry, thereby, represents the geometrical features of the porous body. The trace of S_{ij}/γ_s is equal to the total surface area of the body. The quantity S_{ij}/γ_s was calculated for Ni electrode and pores in the electrode

layer (15 μm × 15 μm) from the nanotomography data in Fig. 4, and was plotted in Fig. 10 (a) and (b), respectively. There was an anisotropy in the surface energy tensor S₃₃/γ_s < S₁₁/γ_s < S₂₂/γ_s. The component S₃₃/γ_s in the thickness direction (the x₃-direction) was the smallest, and the in-plane anisotropy was observed, where the tape casting direction of the BT layer was identified as the x₁-direction for samples sintered at 1150 °C and 1250 °C. The casting direction could not be confirmed for the sample sintered at 1000 °C. Here we assume that the electrode is modeled as a collection of small rectangular plates with thickness t, length L₁ in x₁-axis, and length L₂ in x₂-axis. From Eq. (9), the components of the surface energy tensor are S₁₁/γ_s = N_p(L₁L₂ + L₁t), S₂₂/γ_s = N_p(L₁L₂ + L₂t), S₃₃/γ_s = N_p(L₁ + L₂)t, where N_p is the number of plates. The ratio L₁ : L₂ : t was calculated to be 2.4:1.7:1 and 1.7:1.5:1 for samples sintered at 1150 °C and 1250 °C, respectively. The anisotropy in the surface energy tensor suggests that the model electrode element is a thin rectangular plate with the long side aligned in the tape casting direction.

The anisotropy similar to the electrode was also observed for pores in the material sintered at 1150 °C (Fig. 10 (b)). We approximate the pore structure by a collection of rectangular plate-like pores, then, the ratio L₁ : L₂ : t is 2.1:1.6:1 and 1:1.1:1 for samples sintered at 1150 °C and 1250 °C, respectively. The observed data for 1150 °C indicate that the model pore element is a thin rectangular plate with the long side aligned in the tape casting direction. The in-plane anisotropy in the pore structure disappeared at 1250 °C, where the pore network structure evolved to spherical closed pores. The in-plane anisotropy of pore structures was observed in the viscous sintering of glass film previously [29]. It was suggested that the anisotropy was generated by the tape casting process. The anisotropic pore structure became more isotropic with densification. However, in the processing of MLCC, the electrode was screen printed. It is not clear why both electrode and pore structure in the electrode layer has an in-plane anisotropy which is related to the tape casting direction of the BT layer. Yan reported the in-plane anisotropy in pore orientation of BT layer, and suggested the interaction with the electrode layer and the BT layer [17]. We believe that the same interaction between both layers introduces the in-plane anisotropy in the electrode layer.

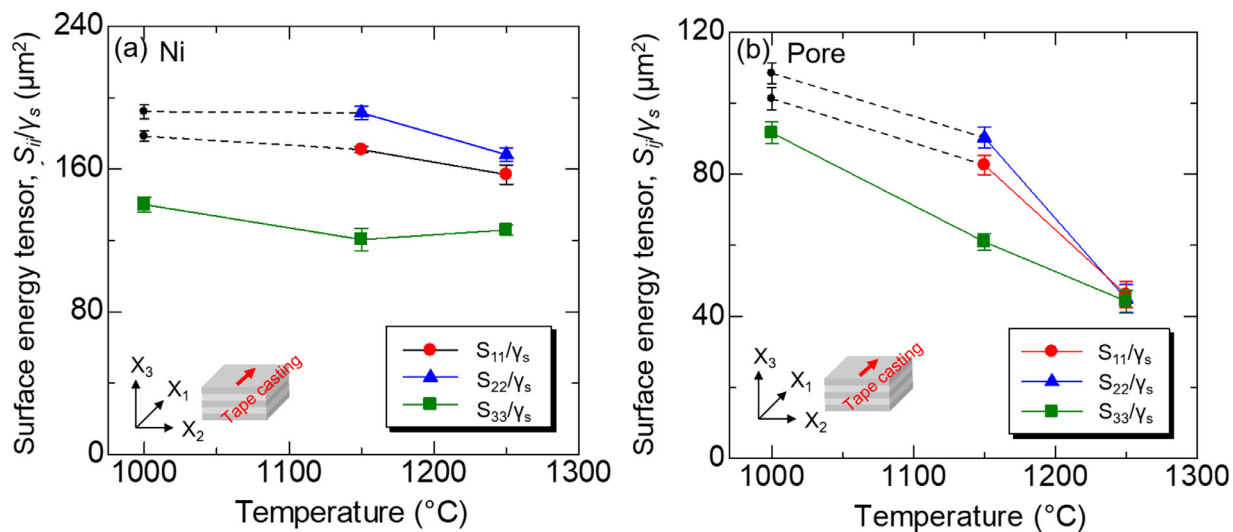


Fig. 10. Anisotropic surface energy tensor of electrode structure. (a) Interface of Ni electrode (Ni/BT + Ni/pores), and (b) pore surface in the electrode layer.

5. Summary

The need for higher capacitance per unit volume leads to multi-layer ceramic capacitor (MLCC) consisting of BaTiO₃ dielectric layer and Ni electrode layer with submicron thickness at the scale of a few particle diameters. As the microstructure of both layers affects capacitance, reliability and lifetime of MLCC, the microstructural evolution during co-sintering was investigated by synchrotron X-ray nano-CT. The thin electrode layer was not continuous, but was porous where Ni regions were connected with ligaments to form complicated network structure. The discontinuous regions were small round holes or irregularly-shaped channels. The ratio of discontinuous area to the total area and the characteristic length of electrode microstructure increased with the sintering temperature; the formation of discontinuity, which brought about capacitance loss, was related to the coarsening process. The coarsening of a hole and the formation of irregularly-shaped channel took place by the coalescence with neighbor holes, breaking up a Ni ligament between them. The relation between the increase of characteristic length and the decrease of total surface/interface area of electrode suggested that the coarsening process was driven by the stress induced instability in addition to the surface tension induced instability. The topological process of ligament pinch-off was indicated as the increase of genus of the electrode, roughly speaking, it is equal to the number of holes. The microstructure evolution of electrode inevitably generated sharp points as a consequence of ligament pinch-off. The characteristic features observed on the electrode surface were the presence of several protrusions or spike-like objects into the dielectric layer, which could enhance the local electric field, thereby, leading to device breakdown. These spikes looked like sharp points formed after the ligament pinch-off.

The effect of the ratio of Ni particle size to electrode thickness on the formation of discontinuity was discussed from the point of view of local fluctuation of packing density in thin electrode layer. The thermodynamics in the sintering of particles of different phases is related to the wetting phenomena. The interaction between nano sized BaTiO₃ particles and Ni particles was discussed from the point of view of wetting phase diagram. The in-plane anisotropy was detected from the analysis of surface energy tensor for the electrode layer. The relation between the anisotropy in the electrode and the casting direction of BT layer suggested the interaction between two layers during co-sintering.

The thermodynamic instability of layered structure under stress is the origin of morphological evolution of electrode. This model predicts that the formation of discontinuity is influenced by the thickness ratio of two layers. The authors believe that the observation of morphological evolution of electrode with different thickness ratio will be a proof of the validity of this model in future.

Declaration of Competing Interest

The authors declare that they have no known competing financial interests or personal relationships that could have appeared to influence the work reported in this paper.

Acknowledgements

The experiment was performed with the approval of JASRI (Proposal No. 2019A1306). This work was supported by JSPS KAKENHI Grant Number JP19K15289.

References

- [1] H. Kishi, Y. Mizuno, H. Chazono, Base-metal electrode-multilayer ceramic capacitors: past, present and future perspectives, *Jpn. J. Appl. Phys.* 42 (2003) 1–15.
- [2] B.-Y. Yu, W.-C.J. Wei, Defects of base metal electrode layers in multi-layer ceramic capacitor, *J. Am. Ceram. Soc.* 88 (2005) 2328–2331.
- [3] M.M. Samantaray, K. Kaneda, W. Qu, E.C. Dickey, C.A. Randall, Effect of firing rates on electrode morphology and electrical properties of multilayer ceramic capacitors, *J. Am. Ceram. Soc.* 95 (2012) 992–998.
- [4] Z. Yan, O. Guillou, S. Wang, C.L. Martin, C.-S. Lee, D. Bouvard, Synchrotron x-ray nano-tomography characterization of the sintering of multilayered systems, *Appl. Phys. Lett.* 100 (2012) 263107.
- [5] F.A. Nichols, W.W. Mullins, Surface- (interface-) and volume-diffusion contributions to morphological changes driven by capillarity, *Trans. Metall. Soc. AIME* 233 (1965) 1840–1848.
- [6] D.J. Srolovitz, On the stability of surfaces of stressed solids, *Acta Metall.* 37 (1989) 621–625.
- [7] N. Sridhar, J.M. Rickman, D.J. Srolovitz, Microstructural stability of stressed lamellar and fiber composites, *Acta Mater.* 45 (1997) 2715–2733.
- [8] N. Sridhar, J.M. Rickman, D.J. Srolovitz, Multilayer film stability, *J. Appl. Phys.* 82 (1997) 4852–4859.
- [9] A.V. Polotai, T.-H. Jeong, G.-Y. Yang, E.C. Dickey, C.A. Randall, P. Pinceloup, A.S. Gurav, Effect of Cr additions on the microstructural stability of Ni electrodes in ultra-thin BaTiO₃ multilayer capacitors, *J. Electroceram.* 18 (2007) 261–268.
- [10] A.V. Polotai, G.-Y. Yang, E.C. Dickey, C.A. Randall, Utilization of multiple-stage sintering to control Ni electrode continuity in ultrathin Ni-BaTiO₃ multilayer capacitors, *J. Am. Ceram. Soc.* 90 (2007) 3811–3817.
- [11] A.V. Polotai, I. Fujii, D.P. Shay, G.-Y. Yang, E.C. Dickey, C.A. Randall, Effect of heating rates during sintering on the electrical properties of ultra-thin Ni-BaTiO₃ multilayer ceramic capacitors, *J. Am. Ceram. Soc.* 91 (2008) 2540–2544.

- [12] H. Chazono, H. Kishi, dc-electrical degradation of the BT-based material for multilayer Ceramic capacitor with Ni internal electrode: impedance analysis and microstructure, *Jpn. J. Appl. Phys.* 40 (2001) 5624–5629.
- [13] G.Y. Yang, E.C. Dickey, C.A. Randall, D.E. Barber, P. Pinceloup, M.A. Henderson, R.A. Hill, J.J. Beeson, D.J. Skamser, Oxygen Nonstoichiometry and dielectric evolution of BaTiO₃, Part I- improvement of insulation resistance with reoxidation, *J. Appl. Phys* 96 (2004) 7492–7499.
- [14] M.M. Samantaray, A. Gurav, E.C. Dickey, C.A. Randall, Electrode defects in multilayer capacitors part I: modeling the effect of electrode roughness and porosity on electric field enhancement and leakage current, *J. Am. Ceram. Soc.* 95 (2012) 257–263.
- [15] J.P. Heath, J.H. Harding, D.C. Sinclair, J.S. Dean, Electric field enhancement in ceramic capacitors due to interface amplitude roughness, *J. Eur. Ceram. Soc.* 39 (2019) 1170–1177.
- [16] Z. Yan, O. Guillon, C.L. Martin, S. Wang, C.-S. Lee, D. Bouvard, In-situ synchrotron x-ray transmission microscopy of the sintering of multilayers, *Appl. Phys. Lett.* 102 (2013) 223107.
- [17] Z. Yan, O. Guillon, C.L. Martin, S. Wang, C.-S. Lee, F. Charlot, D. Bouvard, Correlative studies on sintering of Ni/BaTiO₃ multilayers using X-ray computed nanotomography and FIB-SEM nanotomography, *J. Am. Ceram. Soc.* 98 (2015) 1338–1346.
- [18] O. Sudre, F.F. Lange, The effect of inclusions on densification: III, the desintering phenomenon, *J. Am. Ceram. Soc.* 75 (1992) 3241–3251.
- [19] F. Wakai, F. Aldinger, Equilibrium configuration of particles in sintering under constraint, *Acta Mater.* 51 (2003) 641–652.
- [20] Z. Yan, C.L. Martin, O. Guillon, D. Bouvard, C.S. Lee, Microstructure evolution during the co-sintering of Ni/BaTiO₃ multilayer ceramic capacitors modeled by discrete element simulations, *J. Eur. Ceram. Soc.* 34 (2014) 3167–3179.
- [21] A. Takeuchi, K. Uesugi, M. Uesugi, F. Yoshinaka, T. Nakamura, Nondestructive multiscale X-ray tomography by combining microtomography and high-energy phase-contrast nanotomography, *Microsc. Microanal.* 24 (2018) 106–107.
- [22] G. Okuma, S. Watanabe, K. Shinobe, N. Nishiyama, A. Takeuchi, K. Uesugi, S. Tanaka, F. Wakai, 3D multiscale-imaging of processing-induced defects formed during sintering of hierarchical powder packings, *Sci. Rep.* 9 (2019) 11595.
- [23] V. Buscaglia, C.A. Randall, Size and scaling effects in barium titanate. An overview, *J. Eur. Ceram. Soc.* 40 (2020) 3744–3758.
- [24] K. Sugimura, K. Hirao, Effect of a BaTiO₃ nanoparticle additive on the quality of thin-film Ni electrodes in MLCC, *J. Ceram. Soc. Jpn.* 117 (2009) 1039–1043.
- [25] Y. Kwon, K. Thornton, P.W. Voorhees, The topology and morphology of bicontinuous interfaces during coarsening, *EPL* 86 (2009) 46005.
- [26] Y.K. Chen-Wiegart, S. Wang, Y.S. Chu, W. Liu, I. McNulty, P.W. Voorhees, D.C. Dunand, Structural evolution of nanoporous gold during thermal coarsening, *Acta Mater.* 60 (2012) 4972–4981.
- [27] J. Erlebacher, Mechanism of coarsening and bubble formation in high-genus nanoporous metals, *Phys. Rev. Lett.* 106 (2011) 225504.
- [28] R. Mendoza, K. Thornton, I. Savin, P.W. Voorhees, The evolution of interfacial topology during coarsening, *Acta Mater.* 54 (2006) 743–750.
- [29] F. Wakai, O. Guillon, Evaluation of sintering stress from 3-D visualization of microstructure: case study of glass films sintered by viscous flow and imaged by x-ray microtomography, *Acta. Mater.* 66 (2014) 54–62.
- [30] G. Okuma, D. Kadokawa, T. Hondo, S. Tanaka, F. Wakai, Interface topology for distinguishing stages of sintering, *Sci. Rep.* 7 (2017) 11106.
- [31] Y. Nakano, T. Nomura, T. Takenaka, Residual stress of multilayer ceramic capacitors with Ni-Electrodes (Ni-MLCCs), *Jpn. J. Appl. Phys.* 42 (2003) 6041–6044.
- [32] Y. Konishi, Y. Kowase, K. Hiroi, K. Mizuno, A. Sato, US Patent No. 9,117,590, August 25, 2015.
- [33] B. Lu, S. Torquato, local volume fraction fluctuations in heterogeneous media, *J. Chem. Phys.* 93 (1990) 3452–3459.
- [34] G. Okuma, D. Kadokawa, Y. Shinoda, T. Akatsu, O. Guillon, F. Wakai, Determination of the size of representative volume element for viscous sintering, *J. Ceram. Soc. Jpn.* 124 (2016) 421–425.
- [35] M.R. Razavi, B. Muhunthan, O.A. Hattamleh, Representative elementary volume analysis of sands using X-ray computed tomography, *Geotech. Test. J.* 30 (2007) GTJ100164.
- [36] R.G. Fernandes, S. Selle, T. Wagner, M. Menzel, H. Bornhöft, T. Höche, J. Deubener, Local relative density fluctuation in the early stage of a sintered glass sphere compact determined by X-ray computed tomography, *J. Non-Cryst. Solids* 546 (2020) 120316.
- [37] C. Lin, M.H. Cohen, Quantitative methods for microgeometric modeling, *J. Appl. Phys.* 53 (1982) 4152–4165.
- [38] F. Wakai, D.V. Louzguine-Luzgin, T. Kuroda, A microscopic model of interface-reaction-controlled sintering of spherical particles of different phases, *J. Am. Ceram. Soc.* 92 (2009) 1663–1671.
- [39] S.-F. Wang, T.C.K. Yang, S.-C. Lee, Wettability of electrode metals on barium titanate substrate, *J. Mater. Sci.* 36 (2001) 825–829.
- [40] F. Wakai, Y. Shinoda, Anisotropic sintering stress for sintering of particles arranged in orthotropic symmetry, *Acta Mater.* 57 (2009) 3955–3964.